



Conductance-Controlled Point Functionalization of Single-Walled Carbon Nanotubes

Brett R. Goldsmith, *et al.*

Science **315**, 77 (2007);

DOI: 10.1126/science.1135303

The following resources related to this article are available online at www.sciencemag.org (this information is current as of December 17, 2007):

Updated information and services, including high-resolution figures, can be found in the online version of this article at:

<http://www.sciencemag.org/cgi/content/full/315/5808/77>

Supporting Online Material can be found at:

<http://www.sciencemag.org/cgi/content/full/315/5808/77/DC1>

This article **cites 34 articles**, 2 of which can be accessed for free:

<http://www.sciencemag.org/cgi/content/full/315/5808/77#otherarticles>

This article has been **cited by** 6 article(s) on the ISI Web of Science.

This article appears in the following **subject collections**:

Chemistry

<http://www.sciencemag.org/cgi/collection/chemistry>

Information about obtaining **reprints** of this article or about obtaining **permission to reproduce this article** in whole or in part can be found at:

<http://www.sciencemag.org/about/permissions.dtl>

at various source mass positions revealed source mass-dependent eddy magnetic fields induced by the switching of the MOT coils. After we implemented a controlled decrease of the field (rather than a sudden switch), we no longer saw a statistically significant dependence on the transverse position of the source for deviations as large as 1 cm.

We individually offset other parameters to values beyond accepted operating characteristics of the gradiometer, often to the point at which the interferometer fringe contrast decreased to below $\sim 10\%$ (typical contrast was 25%). These variables included Doppler sensitive π - and $\pi/2$ -pulse lengths, position of atoms in the detection probe beam, detection efficiency, launch angle, off-resonant Raman light, initial $m_f \neq 0$ population (where m_f indicates the Zeeman sublevel), scattering from the background Cs vapor, Raman light intensity, and Raman wavefront quality. Experiments involved the measurement of the Pb-induced phase shift for large offsets in each of the above parameters. At these large offsets, we observed no systematic dependence on the mass displacement signal. From these measurements, we inferred that small drifts of these parameters in time do not contribute systematic offsets in our determination of G .

We looked for systematic effects in our analysis by varying the analysis procedures and parameters. For example, we varied the contrast and outlying phase thresholds used to filter wild points. In this case, we found that for all sets in runs 1 and 2, the inferred values for G agreed to within the statistics. We also studied the effect of the scaling parameters used within the normalized detection scheme to search for possible bias (25). Improper normalization resulted in values for G within statistics, whereas the statistical uncertainties increased for large deviations from optimal parameters.

Our demonstrated proof-of-principle measurement of the Newtonian constant of gravity based on atom interferometric measurement of gravity-induced phase shifts presents a technique for the measurement of G not subject to the known and hidden systematics of previous measurements. Since the completion of this work, the experiment of Tino *et al.* (26) has begun construction of an atom interferometer apparatus with the goal of increasing the sensitivity and decreasing the systematics to perform a measurement of $\delta G/G = 10^{-4}$.

References and Notes

- P. J. Mohr, B. N. Taylor, *Rev. Mod. Phys.* **77**, 1 (2005).
- U. Kleiweß, H. Meyer, A. Schumacher, S. Hartmann, *Meas. Sci. Technol.* **10**, 492 (1999).
- F. Nolting, J. Schurr, S. Schlamminger, W. Kündig, *Meas. Sci. Technol.* **10**, 487 (1999).
- J. P. Schwarz, D. S. Robertson, T. M. Niebauer, J. E. Faller, *Science* **282**, 2230 (1998).
- C. V. Boys, *Philos. Trans. R. Soc.* **186**, 1 (1895).
- P. R. Heyl, P. Chrzanowski, *J. Res. Natl. Bur. Std. U.S.* **29**, 1 (1942).
- G. T. Gillies, *Rep. Prog. Phys.* **60**, 151 (1997).
- P. J. Mohr, B. N. Taylor, *Rev. Mod. Phys.* **72**, 351 (2000).
- J. H. Gundlach, S. M. Merkowitz, *Phys. Rev. Lett.* **85**, 2869 (2000).
- T. J. Quinn, C. C. Speake, S. J. Richman, R. S. Davis, A. Picard, *Phys. Rev. Lett.* **87**, 111101 (2001).
- W. Michaelis, H. Haars, R. Augustin, *Metrologia* **32**, 267 (1995).
- K. Kuroda, *Meas. Sci. Technol.* **10**, 435 (1999).
- W. Michaelis, J. Melcher, H. Haars, *Metrologia* **41**, L29 (2004).
- A. Peters, K. Y. Chung, S. Chu, *Metrologia* **38**, 25 (2001).
- J. M. McGuirk, G. T. Foster, J. B. Fixler, M. J. Snadden, M. A. Kasevich, *Phys. Rev. A* **65**, 033608 (2002).
- P. Berman, Ed., *Atom Interferometry* (Academic Press, New York, 1996).
- K. Bongs, R. Launay, M. A. Kasevich, *Appl. Phys. B* **85**, 602 (2006).
- P. Storey, C. Cohen-Tannoudji, *J. Phys. II* **4**, 1999 (1994).
- M. J. Snadden, J. M. McGuirk, P. Bouyer, K. G. Haritos, M. A. Kasevich, *Phys. Rev. Lett.* **81**, 971 (1998).
- Materials and methods are available as supporting material on Science Online.
- E. L. Raab, M. Prentiss, A. Cable, S. Chu, D. E. Pritchard, *Phys. Rev. Lett.* **59**, 2631 (1987).
- M. Kasevich *et al.*, *Phys. Rev. Lett.* **66**, 2297 (1991).
- J. M. McGuirk, G. T. Foster, J. B. Fixler, M. A. Kasevich, *Opt. Lett.* **26**, 364 (2001).
- G. T. Foster, J. B. Fixler, J. M. McGuirk, M. A. Kasevich, *Opt. Lett.* **27**, 951 (2002).
- Detection-laser powers were periodically adjusted to optimize the detected atom number and signal-to-noise ratio, which results in a slight change of the normalization coefficients, $\alpha_{L,U}$. The normalized $|4,0\rangle$ population is $S_1/(S_1 - \alpha_{L,U}S_2)$, where $S_{1,2}$ is proportional to the $|4,0\rangle$ and $|4,0\rangle - |3,0\rangle$ signal, respectively.
- A. Bertoldi *et al.*, *Eur. Phys. J. D* **40**, 271 (2006).
- This work was supported by grants from the ONR and NASA.

Supporting Online Material

www.sciencemag.org/cgi/content/full/315/5808/74/DC1
Materials and Methods
References

22 September 2006; accepted 22 November 2006
10.1126/science.1135459

Conductance-Controlled Point Functionalization of Single-Walled Carbon Nanotubes

Brett R. Goldsmith,¹ John G. Coroneus,² Vaikunth R. Khalap,¹ Alexander A. Kane,¹ Gregory A. Weiss,^{2,3} Philip G. Collins^{1*}

We used covalent attachments to single-walled carbon nanotubes (SWNTs) to fabricate single-molecule electronic devices. The technique does not rely on submicrometer lithography or precision mechanical manipulation, but instead uses circuit conductance to monitor and control covalent attachment to an electrically connected SWNT. Discrete changes in the circuit conductance revealed chemical processes happening in real time and allowed the SWNT sidewalls to be deterministically broken, reformed, and conjugated to target species. By controlling the chemistry through electronically controlled electrochemical potentials, we were able to achieve single chemical attachments. We routinely functionalized pristine, defect-free SWNTs at one, two, or more sites and demonstrated three-terminal devices in which a single attachment controls the electronic response.

Covalently linking a single molecule of interest between two electrical conductors enables the electrical interrogation of that molecule as it dynamically interacts with the surrounding environment. In practice, however, working single-molecule devices remain exceedingly difficult to fabricate (1). Successes based on very small electrode gaps fabricated lithographically (2), electrically (3, 4), or by scanning probe techniques (5, 6) generally suffer from low fabrication throughput; electrical, mechanical, and chemical instabilities; poorly defined bonding to the molecule of interest; and, sometimes, inconclusive proof that only a single molecule is addressed.

Single-walled carbon nanotubes (SWNTs) have several favorable characteristics for building high-quality, single-molecule devices. Electrically, they are high-conductivity, one-dimensional (1D) conductors that can deliver signals to and from attached molecules. Chemically, SWNTs have long, inert sidewalls but reactive ends to which the tools of organic chemistry can covalently attach a wide variety of species (7). Geometrically, SWNTs' small profile maximizes access to the target molecule by reagents, op-

tical probes, or electrostatic fields. Many strategies for building functioning, nanometer-scale circuits have focused on complex manipulation or high-resolution lithographies (8–11). Guo *et al.*, for example, have beautifully demonstrated single-molecule junctions in broken SWNTs by combining <10 -nm lithography with plasma etching (11).

Here, we describe an alternative technique that does not require high-resolution lithography and is effective for molecules of any size. The general scheme is to fabricate circuits using individual SWNTs and then use the SWNT conductance G as a real-time indicator of SWNT chemical modification. With the use of electrochemically driven reactions, the introduction of functional groups can be electronically controlled and monitored with microsecond tempo-

¹Department of Physics and Astronomy, University of California, Irvine, CA 92697, USA. ²Department of Molecular Biology and Biochemistry, University of California, Irvine, CA 92697, USA. ³Department of Chemistry, University of California, Irvine, CA 92697, USA.

*To whom correspondence should be addressed. E-mail: collinsp@uci.edu

ral resolution, so that point functionalization can be achieved with better than 90% yield.

Our initial experiments were guided by previous studies on highly oriented pyrolytic graphite

crystals (HOPG), as this surface is analogous to the SWNT sidewall. The electrochemical oxidation of HOPG is extensively documented, especially for reactions with strong acids (12). At

moderate oxidative potentials, these acids add delocalized, positive carriers to HOPG; at higher potentials, however, anions react covalently through addition to the carbon sheet. This bonding disrupts the sp^2 carbon network with sp^3 -conjugated carbons, markedly reduces HOPG conductivity, and ultimately leads to the disintegration of HOPG into the insulator graphite oxide (12).

Qualitatively similar effects have been reported for bulk SWNTs (13, 14) but not, to our knowledge, on single, isolated SWNTs, perhaps because of the characterization challenges involved in observing reactions with single- or few-bond resolution (15). However, as shown here, the SWNT's low-bias conductance G is sufficiently sensitive to allow detection. Multiple independent theoretical models have recently calculated G in the presence of single chemical defects, vacancies, or adducts, and have predicted changes (ΔG) on the order of 50% (16–21). The remarkable sensitivity of G to small compositional changes arises from the 1D conductance of SWNTs, which amplifies the effect that a single sp^3 -hybridized carbon can have among 10^6 sp^2 -hybridized carbons. Below, we demonstrate the tremendous sensitivity of G and the potential identification of single-bond chemical events, and describe the use of different functionalization schemes to selectively tailor the resulting sites.

The fabrication and electrochemical modification of samples is discussed in (22) and follows our previous reports (23, 24). Briefly, SWNTs in a narrow diameter range of 1.0 to 1.2 nm are grown by catalyst-assisted chemical vapor deposition (CVD) on thermally oxidized Si wafers. After growth, the SWNTs are contacted by multiple metal electrodes fabricated by optical lithography, and additional lithography is optionally defined on top of the devices to protect the metal and metal-SWNT interfaces with insulating coatings. To prepare them for controlled oxidation, completed devices are mounted in an electrochemical cell (23–26) and contacted by movable probe tips or fixed wirebonds. Platinum counter and reference microelectrodes control the liquid potential (Fig. 1A), although the harsh oxidation conditions require independent calibration of the Pt pseudo-reference against a standard calomel electrode (SCE) in each electrolyte.

The chemical modifications and attachments described below have been tested using Au, Pd, Ti, and TiN electrode metals with and without protective polymethyl methacrylate (PMMA) coatings over the metal. We have determined that the electrode metal and the metal-SWNT interface do not affect the results presented here (22), so we restrict our attention to Ti electrodes unless otherwise noted, as these devices are the least complicated to prepare. The native oxide of the Ti contact metal is sufficient to suppress unwanted electrochemical currents without additional PMMA insulation or lithography (fig. S3) (27).

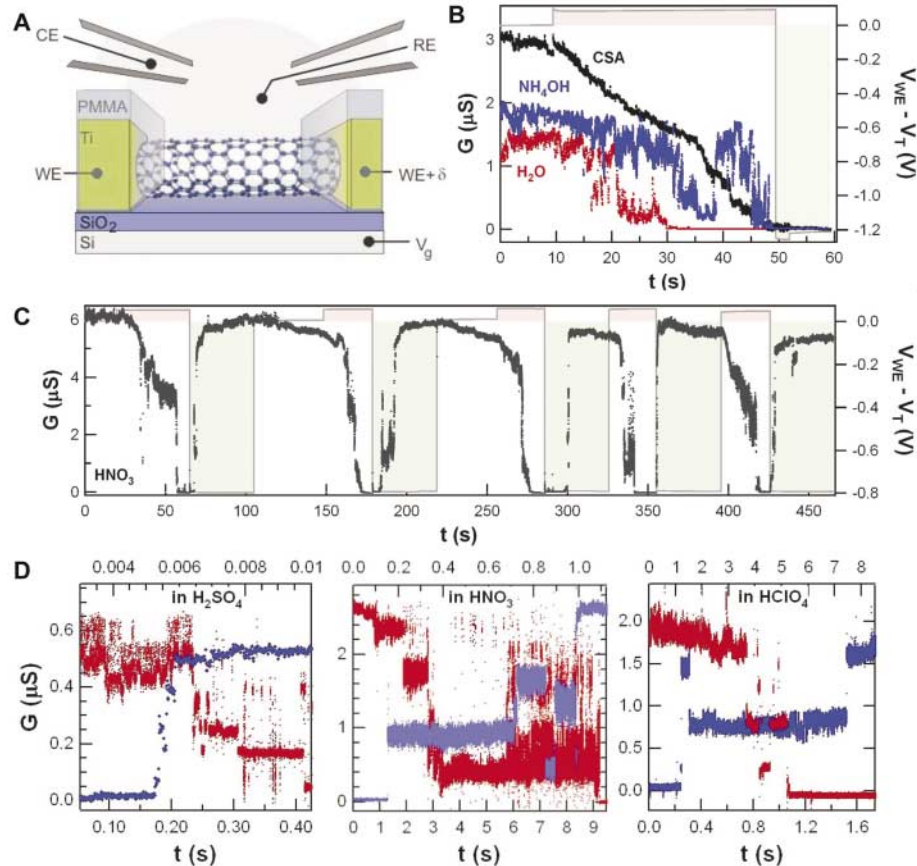


Fig. 1. (A) Schematic of SWNT circuit electrochemical modification. The dynamics of the circuit conductance G during modification differs between electrolytes. CE, counter electrode; RE, reference electrode; WE, working electrode. (B) In most electrolytes, SWNTs oxidize to an open circuit above an electrolyte-dependent threshold V_T (shaded red) and rarely recover under a reducing potential (shaded green). (C) In strong acids, reduction results in nearly complete recovery of conductance and the same SWNT may be redox cycled multiple times. (D) Higher-resolution oxidation (red, lower time scale) and reduction (blue, upper time scale) traces clarify a fine structure of abrupt jumps among metastable intermediate values. Three different strong acids shown here exhibit similar behaviors. All data in (C) and (D) were acquired at 100 kHz. The reduction portions of G in (C) have been scaled up 35% to adjust for the electrostatic gating that occurs at the reducing potential.

Table 1. SWNT electrochemical oxidation characteristics in different electrolytes.

Electrolyte	V_T vs. Pt (V)*	V_T vs. SCE (V)†	ΔV_T (V)	G/G_{init}
HNO ₃ (15.3 M)	0.55	1.6	-0.15	80%
HClO ₄ (7.7 M)	0.70	—	-0.3	90%
H ₂ SO ₄ (18.0 M)	0.80	1.5	-0.1	90%
H ₂ SO ₄ (1.0 M)	0.90	1.4	-0.2	80%
H ₃ PO ₄ (14.7 M)	0.90	—	0	90%
HBr (9.1 M)	0.95	—	0	30%
HCl (12.1 M)	1.10	1.6	0	60%
H ₂ O (deionized)	1.25	1.5	0	60%
KMnO ₄ (6 mM)	0.70	—	—	None
CSA‡ (0.2 M)	1.25	—	—	None
NH ₄ OH (4.3 M)	1.00	1.4	—	None
NaOH (2.6 M)	0.70	1.5	—	None

*All errors are +0.10/-0.05 V except for H₃PO₄ (± 0.2).

†All errors are ± 0.1 .

‡Anhydrous camphorsulfonic acid, in acetonitrile.

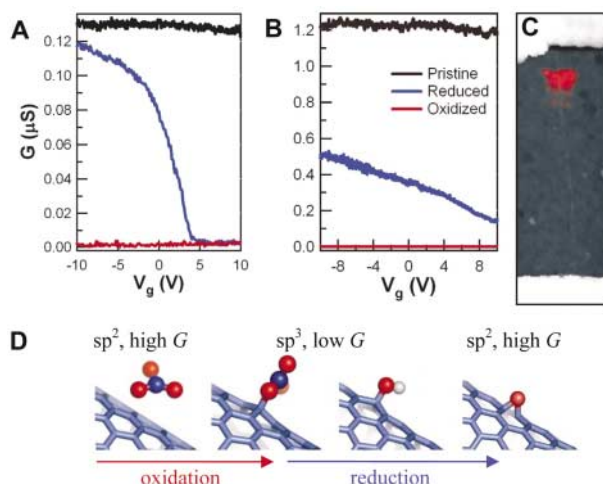
The electrochemical modification of a SWNT is electrolyte-dependent, and Table 1 summarizes the electrolytes tested for this report. In every electrolyte, G is stable across a range of electrochemical potentials, but above an oxidative threshold V_T , the value of G decreases to zero (Fig. 1). Oxidation in bases and weak acids tends to be electrochemically irreversible; Fig. 1B depicts typical results in H_2O , HN_4OH , and nonaqueous camphorsulfonic acid (CSA). On the other hand, the strong acids H_2SO_4 , HNO_3 , $HClO_4$, and H_3PO_4 exhibit a very different behavior in which the application of a reductive potential after oxidation reverses the drop in G (23). This recovery effectively constitutes a redox cycle of the SWNT sidewall and allows the same SWNT to be repeatedly cycled (Fig. 1C). The average degree of recovery is characterized in Table 1 as a percentage of the pristine SWNT's initial G_{init} , but in general the strong acids all behave similarly. We find metallic and semi-conducting SWNTs to have indistinguishable redox behaviors, perhaps because the liquid gate is very effective at moving the Fermi level E_F into the valence band at the large oxidative potentials used here (25, 26). We also note that variability in V_T is primarily caused by chemical instabilities of the Pt microreference, so that within the experimental error it is a constant $V_T = 1.6 \pm 0.1$ V versus SCE. This value may represent the true oxidation threshold of defect- and edge-free graphene, and as such it slightly exceeds what can be achieved with high-quality HOPG (28, 29).

In both reversible and irreversible electrolytes, the dynamics of the SWNT failure are revealing. Precisely biased just below the threshold V_T , G decreases continuously in time before stabilizing near $0.7G_{init}$. More typically, coarse potentiostat control will exceed V_T , and in this case G continues its decrease through a complex sequence of abrupt, discrete steps. These steps are most reliably observed in the strong acids (Fig. 1,

C and D). During both oxidation (red) and subsequent reduction (blue), $G(t)$ repeatedly samples and stabilizes at discrete conductance values, then jumps among these values in a period equal to or less than the temporal resolution of the data (10 μ s). The intermediate terraces during oxidation exhibit excellent alignment with those during reduction, with little indication of anion dependence (19). Although such good alignment is not observed in every measurement, the reduction and oxidation traces frequently have similar numbers of terraces and step heights (ΔG). The different time scales used for each trace in Fig. 1D indicate the degree to which the chemical processes are sensitive to the applied voltages once a reaction threshold is exceeded.

In either the oxidized or reduced state, no structural damage was observed on these SWNTs within the resolution limits of atomic force microscopy (AFM), and this finding, combined with the redox reversibility, rules out the possibility that carbon atoms are being permanently removed from the SWNT. Instead, we interpret the changes in G to be indicative of the same chemistries that occur on HOPG, except amplified by the 1D nature of a SWNT. The initial, continuous changes in G can be attributed to charge transfer-induced disorder and the discrete steps to covalent oxidation (12–14). The short time required for one step ΔG to occur and the long latencies between steps suggest a stochastic process consistent with individual oxidation events; the step heights observed are consistent with the theoretical predictions for such events (16–21). We conclude that each step likely corresponds to the formation of a single covalent C-O bond between the SWNT and the nitrate, sulfate, or other conjugate base, in the same ways that such anions form adducts with the HOPG basal plane (12). The detailed dynamics and metastability in G then likely reflect the different leaving-group abilities for the elimination reaction.

Fig. 2. (A and B) After a single redox cycle, metallic SWNTs show strong V_g dependences. $G(V_g)$ is flat before oxidation (black), zero after oxidation (red), and then semiconductor-like after reduction (blue). Subsequent cycles have lesser effects on G , but flat $G(V_g)$ curves were never recovered. It is also common for the G recovery to be incomplete in metallic SWNTs (B). **(C)** A composite of AFM topography in grayscale and SGM in red identifies a local region responsible for the gate sensitivity of the device in (A). **(D)** Proposed chemical process for HNO_3 oxidation and reduction, in which the redox cycle is not fully reversible but instead leaves behind a C-OH or C-O-C residue. The latter has sp^2 conjugation and restores the SWNT conductivity.



Despite the apparent reversibility of the cycling, multiple redox cycles on the same SWNT result in both random and gradual degradation, even in the best electrolytes. For example, Fig. 1C shows a 20% degradation after five redox cycles in HNO_3 . We have extensively studied SWNTs before and after single redox cycles and have identified the cause of this degradation: Residual SWNT modifications remain even when G recovers to $>0.9G_{init}$. The first indication of this residual damage is a small, one-time threshold reduction ΔV_T that occurs between the first and all subsequent redox cycles. This shift indicates that subsequent oxidation can take advantage of some residual disorder and/or enhanced reactivity.

Second, we observe a substantial change in the electronic behavior of every metallic SWNT measured. Normally, the G of a metallic SWNT is insensitive to a nearby gate electrode biased at voltage V_g . As shown in Fig. 2, A and B, single redox cycles electronically alter metallic SWNTs and make them gate-sensitive. Experimentally and theoretically, it has been established (30–32) that a point defect embedded in a metallic SWNT can cause this V_g modulation.

Third, we have used scanning probe techniques to investigate SWNTs before and after redox cycling. Although the residual disorder is topologically invisible, scanning gate microscopy (SGM) and Kelvin force microscopy (KFM) can resolve it (33). SGM is a technique in which V_g is locally applied with an AFM cantilever to a small region of a SWNT. The resulting map of $G(V_g)$ spatially identifies any SWNT regions that contribute to gate sensitivity. Figure 2C is an AFM image of a metallic SWNT and, in false color, its SGM map showing a V_g -sensitive site added by redox cycling. We observe the introduction of similar sites to semiconducting SWNTs, although in this case the change in $G(V_g)$ is naturally smaller than in Fig. 2A. Finally, we observe that annealing the redox-cycled samples (400°C in vacuum or N_2) fully restores both the initial $G(V_g)$ and the oxidation threshold V_T .

We conclude that electrochemical reduction does not return a SWNT to its pristine chemical state, despite the near-perfect recovery in G . Instead, reduction further alters the SWNT's chemical state at one or more sites. Because of the limited active area, we have been unable to directly detect the resulting chemical functionalities by common optical spectroscopies, but identical acid oxidation produces adducts such as hydroxides, epoxides, and ethers on HOPG and bulk SWNTs (12–14). Of these, divalent ethers are a particularly attractive candidate for the redox-cycled SWNTs because they have been predicted to minimally affect G (21, 34, 35). Whereas other functionalities produce sp^3 hybridizations, the ethers have sp^2 carbons that only weakly scatter free carriers. Figure 2D outlines a scheme adopted from HOPG in which a strong acid oxidizes the SWNT sidewall and, upon subsequent reduction, leaves behind the ether functionalization.

Regardless of the exact chemical pathway, the residual sites provide a chemical handle for further sidewall functionalization. Additional

reactions can be promoted on either the oxidized or reduced SWNTs. However, the stochastic nature of the original damage means that these

reactions will tailor a very limited number of functionally active sites. Thanks to the sensitivity of G , electronic triggering can give ready control over the degree of covalent oxidation, and the electrolyte used can provide flexible control over the functional adducts.

For example, further oxidation of SWNTs has been tested in aqueous KMnO_4 (6.5 mM). Pristine SWNT devices are unaffected when exposed to KMnO_4 . Furthermore, performing a single oxidation-reduction cycle in acid is usually insufficient to make a SWNT reactive with KMnO_4 . Alternatively, SWNTs that have been oxidized but not reduced are irreversibly changed by exposure to KMnO_4 for 30 s. These devices do not conduct at low bias, even after electrochemical reduction, and thermal annealing only partially recovers the device characteristics. Careful examination of $G(t)$ traces acquired before, during, and after KMnO_4 application can prevent accidental reduction before KMnO_4 reaction. Figure 3A shows a typical $G(V_g)$ characteristic of a metallic SWNT before modification, after acid and KMnO_4 oxidation, and then after thermal annealing. The new gate sensitivity in the device can be mapped by SGM to a local region of the SWNT sidewall (Fig. 3B). The complementary technique of KFM, in which the electrostatic potential of the SWNT is mapped, shows a potential drop in the same region (Fig. 3C).

We have also performed selective electrochemical deposition, a technique specially designed to label point defects on the basis of their enhanced reactivity (24). Pristine SWNTs found to have no electrochemically active sites were routinely labeled by selective Ni deposition after a redox cycle, and this labeling usually occurred at a single site (22). More remarkably, Ni could be deposited on open-circuit SWNTs that had been oxidized with KMnO_4 . In this case, the Ni deposit is not only visible (Fig. 3D) but also reconnects the electrical circuit. Figure 3E shows $G(V_g)$ electrical characterization of a semiconducting SWNT before and after oxidation and then after Ni deposition. The oxidation decreases G by a factor of 1000, producing a characteristic behavior similar to gap tunneling (23). Nickel deposition closes this tunneling gap (but does not affect the SWNTs' semiconducting band structure) to reproduce the initial $G(V_g)$ behavior but with a higher on-state resistance. Kept in air, these devices become insulating again as the Ni deposition oxidizes, but storage in vacuum stabilizes the electrical characteristics indefinitely.

The electrochemical and scanning probe techniques have resolution limits of 5 and 50 nm, respectively, and cannot distinguish between single- and multiple-bond disruptions to the SWNT, but they do rule out randomly distributed or widely spaced damage. Furthermore, the presence of an oxygen-containing functionality is virtually certain, given that Ni deposition proceeds with nearly 100% yield. Reactions with higher chemoselectivity are required to achieve

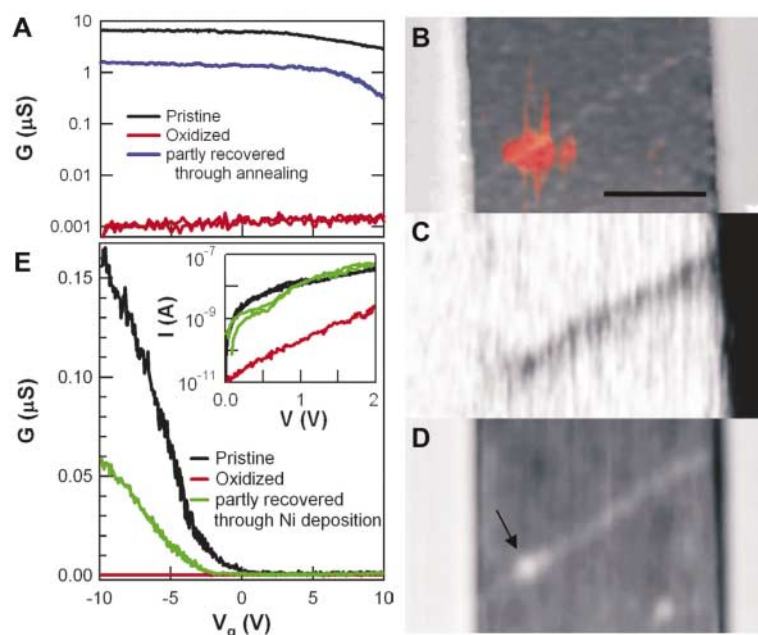


Fig. 3. (A) $G(V_g)$ for a quasi-metallic SWNT electrochemically oxidized and exposed to KMnO_4 (red). The additional KMnO_4 oxidation permanently damages the SWNT, so that even thermal annealing does not fully recover G (blue). (B) A composite of AFM topography (grayscale) and SGM (red) identifies the region responsible for the enhanced gate sensitivity of an oxidized SWNT. (C) KFM imaging shows that most of the potential applied across the SWNT is dropped across this gate-sensitive region. (D) Selective electrodeposition of Ni identifies this site as more chemically reactive than the rest of the SWNT. Scale bar, 500 nm. (E) A similar experiment on a semiconducting SWNT in which the device is open-circuited before Ni deposition and conducting afterward (green). $G(V_g)$ reflects the SWNT band structure as well as the extra resistance associated with the Ni-coated, oxidized region. Inset shows corresponding current-voltage characteristics.

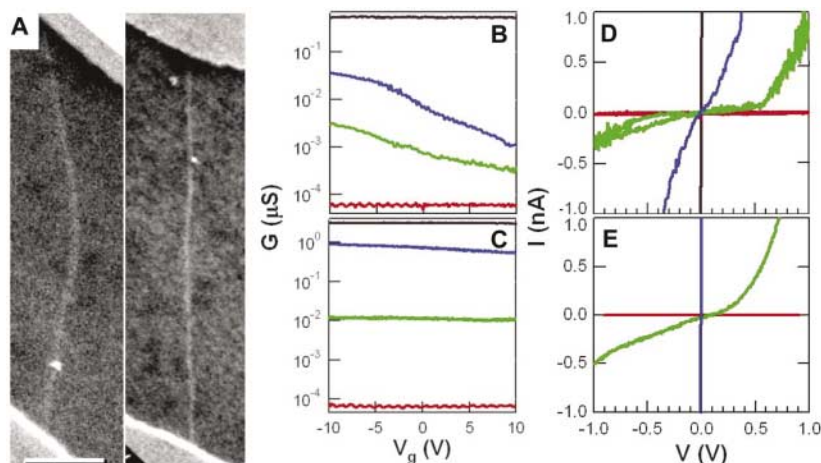


Fig. 4. (A) Scanning electron micrographs of SWNT devices incubated with streptavidin after controlled oxidation. Streptavidin covalently binds to each oxidation site, which has been activated by treatment with EDC and NHS. Nonspecific adsorption is minimized by a polysorbate surfactant. Each SWNT is visible because it is a conductor sitting on an insulating surface; the proteins are not visible but are labeled with 20-nm Au particles for imaging. Scale bar, 500 nm. (B and C) $G(V_g)$ curves at each stage in the chemical treatment show the pristine (black curves), oxidized (red), and protein-conjugated (green) chemical states, with a substantial recovery in conductance upon successful conjugation. (D and E) The corresponding current-voltage curves show decidedly nonlinear behaviors. Note that the high-conductance states (black, blue) and the oxidized, low-conductance state (red) overlap the graphs' axes. Thermal annealing of the samples does not fully recover any of the conjugated SWNT devices (blue curves).

higher resolution and further discriminate among possible chemical modifications.

For example, the highly chemoselective activation of carboxyl groups by treatment with *N*-ethyl-*N'*-(3-dimethyl aminopropyl) carbodiimide (EDC) and *N*-hydroxysuccinimide (NHS) is used to attach proteins to carboxy-terminated surfaces via amide linkages (36). In a third series of chemical experiments, redox-cycled SWNTs were treated with EDC and NHS in an attempt to covalently link Au-labeled streptavidin to SWNT carboxyls (37). Only one attachment was observed on 10 redox-cycled SWNT devices, which shows that the acid treatment does not generally produce sidewall carboxy groups. This result is in agreement with our speculation that ethers are the dominant residual functionality. However, four of nine devices showed protein attachments when additional KMnO_4 oxidation was added to the procedure. KMnO_4 readily converts hydroxides to carboxy groups, so we can conclude with some certainty that the electronic maps in Fig. 3, B and C, are related to carboxy-functionalized sites.

Figure 4A and fig. S5A show scanning electron micrographs of successful protein attachments. In each image, a single streptavidin-coated Au particle is integrated into a functioning SWNT device. Electrical characterization of these devices shows that each circuit is insulating immediately before streptavidin attachment but conducting afterward (Fig. 4, B to E). *G* is critically dependent on the presence of the protein, just as in the case of the Ni decorations, even though the current does not flow through the entire protein or gold particle per se. As in Fig. 3E, the measured *G* reflects the series combination of SWNT band structure and protein-linked oxidation gaps, and these devices could

exhibit strong biosensitivity, as previously shown for noncovalently coated SWNTs (38).

The usefulness of *G* to monitor and control chemistry in situ and in real time arises from its sensitivity to a few single-bond redox events. Paradoxically, SWNT devices never drop directly to $G = 0$ without intermediate steps and terraces, and questions remain regarding the exact nature of these terraces. Additional experiments may distinguish among intermediate chemical states, oxidation cascades among neighboring carbon atoms, or other possible mechanisms.

References and Notes

1. G. Maruccio *et al.*, *Electroanalysis* **16**, 1853 (2004).
2. A. A. Tseng, A. Notargiacomo, T. P. Chen, *J. Vac. Sci. Technol. B* **23**, 877 (2005).
3. H. Park, A. K. L. Lim, A. P. Alivisatos, J. Park, P. L. McEuen, *Appl. Phys. Lett.* **75**, 301 (1999).
4. D. R. Strachan *et al.*, *Appl. Phys. Lett.* **86**, 43109 (2005).
5. W. Ho, *J. Chem. Phys.* **117**, 11033 (2002).
6. N. J. Tao, *J. Mater. Chem.* **15**, 3260 (2005).
7. S. Banerjee, T. Hemraj-Benny, S. S. Wong, *Adv. Mater.* **17**, 17 (2005).
8. P. W. Chiu, G. S. Duesberg, U. Dettlaff-Weglikowska, S. Roth, *Appl. Phys. Lett.* **80**, 3811 (2002).
9. Y. X. Zhou, A. T. Johnson, J. Hone, W. F. Smith, *Nano Lett.* **3**, 1371 (2003).
10. M. R. Diehl *et al.*, *ChemPhysChem* **4**, 1335 (2003).
11. X. Guo *et al.*, *Science* **311**, 356 (2006).
12. K. Kinoshita, *Carbon—Electrochemical and Physicochemical Properties* (Wiley Interscience, New York, 1988).
13. G. U. Sumanasekera *et al.*, *J. Phys. Chem. B* **103**, 4292 (1999).
14. R. Graupner *et al.*, *Phys. Chem. Chem. Phys.* **5**, 5472 (2003).
15. M. Burghard, *Surf. Sci. Rep.* **58**, 1 (2005).
16. X. Lu, Z. F. Chen, *Chem. Rev.* **105**, 3643 (2005).
17. J. Zhao *et al.*, *ChemPhysChem* **6**, 598 (2005).
18. Y. W. Son, J. Ihm, M. L. Cohen, S. G. Louie, H. J. Choi, *Phys. Rev. Lett.* **95**, 216602 (2005).
19. Y. S. Lee, M. B. Nardelli, N. Marzari, *Phys. Rev. Lett.* **95**, 076804 (2005).

20. J. Eom *et al.*, *Physica B* **376–377**, 7 (2006).
 21. Y.-S. Lee, N. Marzari, *Phys. Rev. Lett.* **97**, 116801 (2006).
 22. See supporting material on Science Online.
 23. J. Mannik, B. R. Goldsmith, A. Kane, P. G. Collins, *Phys. Rev. Lett.* **97**, 016601 (2006).
 24. Y. Fan, B. R. Goldsmith, P. G. Collins, *Nat. Mater.* **4**, 906 (2005).
 25. M. Krüger, M. R. Buitelaar, T. Nussbaumer, C. Schonenberger, L. Forro, *Appl. Phys. Lett.* **78**, 1291 (2001).
 26. S. Rosenblatt *et al.*, *Nano Lett.* **2**, 869 (2002).
 27. I. Heller *et al.*, *Nano Lett.* **5**, 137 (2005).
 28. J. O. Besenhard, H. Mohwald, J. J. Nickl, *Synth. Met.* **3**, 187 (1981).
 29. A. Metrot, J. E. Fischer, *Synth. Met.* **3**, 201 (1981).
 30. M. Bockrath *et al.*, *Science* **291**, 283 (2001).
 31. S. J. Tans, C. Dekker, *Nature* **404**, 834 (2000).
 32. M. Freitag, A. T. Johnson, S. V. Kalinin, D. A. Bonnell, *Phys. Rev. Lett.* **89**, 216801 (2002).
 33. A. Bachtold *et al.*, *Phys. Rev. Lett.* **84**, 6082 (2000).
 34. H. Park, J. J. Zhao, J. P. Lu, *Nanotechnology* **16**, 635 (2005).
 35. H. Pan, Y. P. Feng, J. Y. Lin, *Phys. Rev. B* **70**, 245425 (2004).
 36. J. V. Staros, R. W. Wright, D. M. Swingle, *Anal. Biochem.* **156**, 220 (1986).
 37. S. S. Wong, E. Joselevich, A. T. Woolley, C. L. Cheung, C. M. Lieber, *Nature* **394**, 52 (1998).
 38. A. Star, J. C. P. Gabriel, K. Bradley, G. Gruner, *Nano Lett.* **3**, 459 (2003).
19. We thank J. Mannik and F. Alim for experimental assistance, and our team collaborators R. Penner and N. Albritton for helpful conversations. Supported by NSF NIRT grant EF-0404057, NSF CAREER grant DMR-023-9842 (P.G.C.), American Chemical Society Petroleum Research Fund grant 39672-G5M (P.G.C.), National Institute of General Medical Sciences grant R01 GM078528-01 (G.A.W.), and National Institute of Allergy and Infectious Diseases grant R43 AI58365-01 (G.A.W.).

Supporting Online Material

www.sciencemag.org/cgi/content/full/315/5808/77/DC1
Materials and Methods
SOM Text
Figs. S1 to S5

19 September 2006; accepted 7 November 2006
10.1126/science.1135303

Counting Low-Copy Number Proteins in a Single Cell

Bo Huang,^{1*} Hongkai Wu,^{1†} Devaki Bhaya,² Arthur Grossman,² Sebastien Granier,³ Brian K. Kobilka,³ Richard N. Zare^{1‡}

We have designed a microfluidic device in which we can manipulate, lyse, label, separate, and quantify the protein contents of a single cell using single-molecule fluorescence counting. Generic labeling of proteins is achieved through fluorescent-antibody binding. The use of cylindrical optics enables high-efficiency ($\approx 60\%$) counting of molecules in micrometer-sized channels. We used this microfluidic device to quantify β_2 adrenergic receptors expressed in insect cells (SF9). We also analyzed phycobiliprotein contents in individual cyanobacterial cells (*Synechococcus* sp. PCC 7942) and observed marked differences in the levels of specific complexes in cell populations that were grown under nitrogen-depleted conditions.

Single-cell analysis has become a highly attractive tool for investigating cellular contents (1). Unlike conventional methods that are performed with large cell populations, this technology avoids the loss of information associated with ensemble averaging. Recent studies have described methods that can quantify specific proteins inside a single cell (2–4) by means of

integrated fluorescence (including confocal microscopy, flow cytometry, and monitoring fluorescent enzymatic products) and, in another instance (5), by single-molecule imaging. These techniques restrict analysis to one or perhaps a few species at a time because of the need to resolve fluorescence from different probes. Moreover, their applications are limited in the cases where the cell environment

changes the fluorescence of the reporter molecule (e.g., through quenching or resonance energy transfer) or where endogenous fluorescence interferes with the measurements.

We present a different approach based on manipulating, capturing, and lysing a single cell, followed by chemical separation and analysis of the lysate. This approach sacrifices the possibility of monitoring live cells but gains the ability to quantify multiple targets that cannot be distinguished by fluorescence properties alone. Recent achievements—including the analysis of DNA (6), amino acid profiles (7), and protein fingerprints (8)—use either a capillary or a mi-

¹Department of Chemistry, Stanford University, Stanford, CA 94305-5080, USA. ²Department of Plant Biology, Carnegie Institution, Stanford, CA 94305, USA. ³Department of Molecular and Cellular Physiology and Medicine, Stanford University, Stanford, CA 94305-5345, USA.

*Present address: Department of Chemistry and Chemical Biology, Harvard University, Cambridge, MA 02138, USA.

†Present address: Department of Chemistry, Tsinghua University, Beijing 100084, China.

‡To whom correspondence should be addressed. E-mail: zare@stanford.edu